

# Research on the visual/inertial integrated carrier landing guidance algorithm

Yue Meng<sup>1</sup>, Wei Wang and Zhenxing Ding

## Abstract

In this article, we describe a visual/inertial integrated carrier landing guidance algorithm for aircraft carrier landing operations. The airborne vision system and the inertial navigation system are employed as sensors to obtain feature points of carrier runway as well as the aircraft inertial measurements. In this algorithm, visual and inertial information are integrated, and the Pose from Orthographic Projection and Scaling with Iterations algorithm is utilized to estimate aircraft position and carrier motion. A simulation was constructed validating this algorithm, and the results of this simulation show satisfactory accuracy as well as high efficiency in carrier landing guidance.

## Keywords

Carrier landing guidance, vision, inertial, POSIT

Date received: 12 May 2017; accepted: 7 February 2018

Topic: Vision Systems

Topic Editor: Antonio Fernandez-Caballero

Associate Editor: Grazia Cicirelli

## Introduction

The carrier-borne aircraft is one of the most important constituents of the aircraft carrier. However, the complex landing environment can potentially lead to a landing failure because of a small landing area, carrier motion, and occasional conditions of low visibility.<sup>1</sup> Aircraft carrier landing is one of the most difficult operational challenges in the world.

For a safe landing operation, various kinds of landing guidance systems are developed for guiding aircraft to follow accurate slope–slide path and reach touchdown position, such as a shipboard tracking radar system<sup>2,3</sup> and Shipboard Relative Global Positioning System.<sup>4,5</sup> These guidance systems can meet the typical carrier landing requirements but lack guidance capacity when wireless communication cannot function.

With the development of photoelectric technology, the airborne vision-guided technology, which can be considered as an autonomous navigation technology, has attracted attention in aircraft landing research. Sharp et al.<sup>6</sup> and Saripalli et al.<sup>7</sup> used specially designed planar features to land a helicopter. In the work of Gui et al.,<sup>8</sup> maximum

between-class variance algorithm, region growing algorithm, and negative Laplacian of Gaussian operator are used to detect and track centers of the infrared lamps in the images. In a previous study,<sup>9</sup> the runway boundary lines were extracted using Hough transforms, and the lateral offset of the unmanned aerial vehicle (UAV) was estimated with respect to the runway centerline. All these methods can be applied to landing on an aircraft carrier. In the work of Yakimenko et al.,<sup>10</sup> three infrared points were used to calculate the relative position and orientation of a UAV with respect to a ship. A three-dimensional (3-D) model-based tracker was used to estimate the camera poses, and their detection targets are a warped patch of a reference image,

School of Instrumentation Science and Opto-electronics Engineering,  
Beihang University, Beijing, China

## Corresponding author:

Wei Wang, School of Instrumentation Science and Opto-electronics Engineering, Beihang University, No. 37, Xueyuan Road, Haidian District, Beijing 100191, China.

Email: wongwei@buaa.edu.cn



three visual features including two white triangles on the runway and a white line along the stern.<sup>11,12</sup> However, the methods mentioned above cannot estimate the ship motion, and their results can potentially be improved for greater accuracy. Ding et al.<sup>13</sup> estimated the ship motion using Newton's iterative algorithm, but there is still room for improvement in terms of accuracy and efficiency.

This article presents a visual/inertial integrated carrier landing guidance algorithm that requires less execution time as well as eliminates the need for Jacobian determinant calculation in Newton's iterative algorithm. In this algorithm, the Pose from Orthographic Projection and Scaling with Iterations (POSIT) algorithm is utilized to estimate the relative position and attitude between the aircraft and the carrier from visual information, and the carrier motion can be decoupled by using the aircraft attitude information from the airborne inertial navigation system (INS). Then, the changing position of the landing point caused by carrier motion can be estimated, and the optimal trajectory can be planned according to the height of the landing point. The position of the aircraft deviating from the optimal trajectory is calculated and delivered to the aircraft control system. A simulation is constructed to validate the performance of the algorithm.

This article is organized as follows. An overview of the visual/inertial integrated landing guidance system, the mathematical model, and the details of the landing guidance algorithm are presented in the "Materials and methods" section, followed by simulation and comparison of the results in the "Simulation" section, and finally, concluding remarks in the "Conclusion" section.

## Materials and methods

### System overview

We consider an infrared system as the airborne vision system. The infrared system is installed in front of the aircraft, and four infrared cooperated targets are set on the deck for carrier identification and location. Other common vision systems can also apply the method discussed in this article for the pose estimation after completing the recognition of characteristic points.

The schematic of system is shown in Figure 1. The four red points represent the four cooperated targets that are set on the deck for visual detection.

The vision system gauges the image of the runway containing cooperated targets and utilizes image recognition methods such as the maximum between-class variance algorithm,<sup>8</sup> edge extraction based on Canny operator, and contour-based moment algorithm to recognize the image coordinates of the targets' centers. There are one-to-one relationships between the two-dimensional (2-D) infrared image coordinates on the vision system and the real 3-D position of infrared cooperated targets on the carrier. Through this relationship, the POSIT algorithm calculates

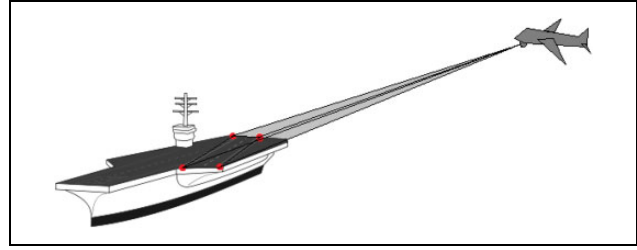


Figure 1. The vision system and the cooperated targets.

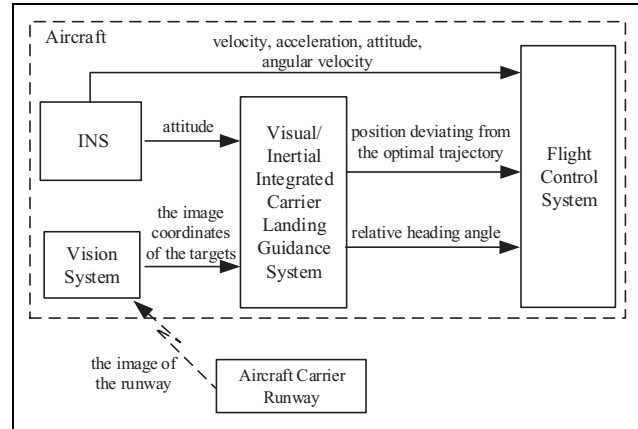


Figure 2. The visual/inertial integrated carrier landing guidance system block diagram.

the relative pose between the aircraft and the carrier. By integrating the aircraft attitude measurements from the INS, the carrier motion can be decoupled from the relative pose information and then utilized to calculate a reference flight path. All landing guidance information is delivered to the flight control system (FCS) for controlling the aircraft.

The complete block diagram for the carrier landing guidance system is shown in Figure 2.

### Coordinate system

The aircraft carrier is assumed to be at sailing straight with typical roll, pitch, and heave dynamics, which have considerable influence on the position of landing point. The aircraft is gliding to the expected landing point with a horizontal angle of  $3.5^\circ$ .

The frames involved are shown in Figure 3. All coordinate systems are right-handed. The frame  $F_O$  is defined as the navigation coordinate, where the  $y$ -axis coincides with the runway centerline and the  $z$ -axis points upward. The aircraft body frame  $F_B$  and the carrier body frame  $F_S$  are designed with the  $z$ -axis oriented upward and the  $y$ -axis pointing to the head. The carrier runway frame  $F_R$  corresponds to the expected landing point on the carrier deck, translated by the offset vector  ${}^S_R T^R$  and rotated around its  $z$ -axis expressed as matrix  ${}^S_R R^R$  from the carrier frame  $F_S$ . The camera frame  $F_C$  corresponds to the origin of the camera, translated by the offset vector  ${}^B_C T^C$  and rotated around

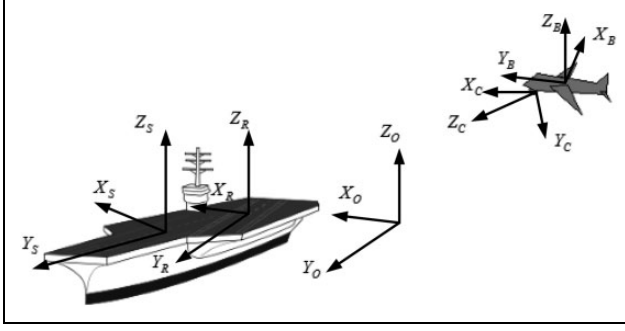


Figure 3. Coordinate system.

its  $x$ -axis expressed as the matrix  ${}^C R^B$  from the aircraft body frame.

The pose of the aircraft and the aircraft carrier in  $F_O$  are, respectively, defined as

$${}^O p_B = ({}^O x_B, {}^O y_B, {}^O z_B)^T, \quad {}^O \Phi = ({}^O \theta_B, {}^O \gamma_B, {}^O \psi_B)^T \quad (1)$$

and

$${}^O p_S = ({}^O x_S, {}^O y_S, {}^O z_S)^T, \quad {}^O \Phi = ({}^O \theta_S, {}^O \gamma_S, {}^O \psi_S)^T \quad (2)$$

where  ${}^O p_B$  and  ${}^O p_S$  represent the relative positions;  ${}^O \Phi$  and  ${}^O \Phi$  are Euler angles for relative attitudes;  ${}^O \theta_B$ ,  ${}^O \gamma_B$ , and  ${}^O \psi_B$  are the pitch, roll, and heading angles of the aircraft in the navigation frame, respectively; and  ${}^O \theta_S$ ,  ${}^O \gamma_S$ , and  ${}^O \psi_S$  are the pitch, roll, and heading angles of the aircraft carrier in the navigation frame, respectively.

The coordinates of the four infrared cooperated targets are expressed as  ${}^R p_{ig} = (x_{ir}, y_{ir}, z_{ir})^T$  ( $i = 1, 2, 3, 4$ ) in  $F_R$ . Thus, those coordinates in different frames can be calculated as follows

$${}^S p_{ig} = {}^S R \cdot {}^R p_{ig} + {}^S T \quad (3)$$

$${}^O p_{ig} = {}^O S \cdot {}^S p_{ig} + {}^O T = R_z(-{}^O \psi_S) \cdot R_x(-{}^O \theta_S) \cdot R_y(-{}^O \gamma_S) \cdot {}^S p_{ig} + {}^O p_S \quad (4)$$

$${}^B p_{ig} = {}^B O R \cdot ({}^O p_{ig} - {}^O T) = R_y({}^O \gamma_B) \cdot R_x({}^O \theta_B) \cdot R_z({}^O \psi_B) \cdot ({}^O p_{ig} - {}^O p_B) \quad (5)$$

$${}^C p_{ig} = (x_{ic}, y_{ic}, z_{ic})^T = {}^C B R \cdot ({}^B p_{ig} + {}^B T) \quad (6)$$

where  ${}^S p_{ig}$ ,  ${}^O p_{ig}$ ,  ${}^B p_{ig}$ , and  ${}^C p_{ig}$  are the coordinates of the targets in the carrier body frame, navigation frame, aircraft body frame, and camera frame, respectively.  $R_x(\cdot)$ ,  $R_y(\cdot)$ , and  $R_z(\cdot)$  are the functions to calculate the rotation matrix that helps rotate a vector around the  $x$ -axis,  $y$ -axis, and  $z$ -axis with an angle of  $\cdot$ . For example, equation (4) can be expanded as follows

$$\begin{bmatrix} x_{io} \\ y_{io} \\ z_{io} \end{bmatrix} = \begin{bmatrix} \cos {}^O \psi_S & -\sin {}^O \psi_S & 0 \\ \sin {}^O \psi_S & \cos {}^O \psi_S & 0 \\ 0 & 0 & 1 \end{bmatrix} \cdot \begin{bmatrix} 1 & 0 & 0 \\ 0 & \cos {}^O \theta_S & -\sin {}^O \theta_S \\ 0 & \sin {}^O \theta_S & \cos {}^O \theta_S \end{bmatrix} \cdot \begin{bmatrix} x_{is} \\ y_{is} \\ z_{is} \end{bmatrix} + \begin{bmatrix} {}^O x_S \\ {}^O y_S \\ {}^O z_S \end{bmatrix}$$

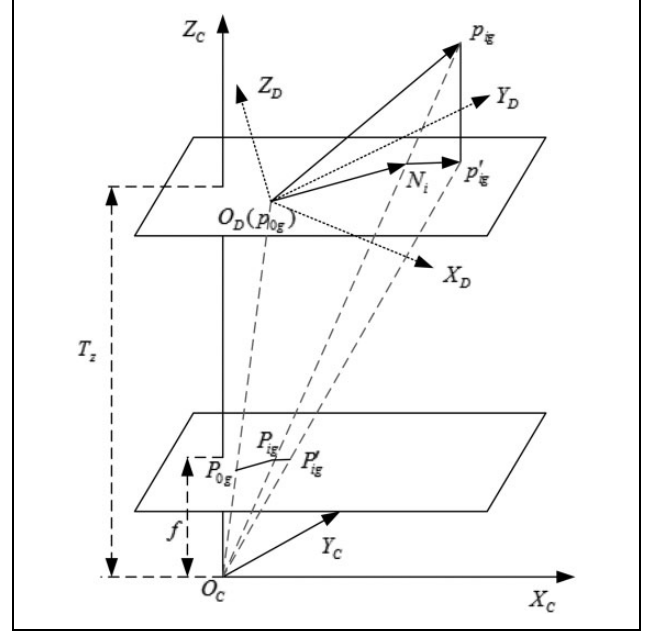


Figure 4. Perspective projection and scaled orthogonal projection.

$$\begin{bmatrix} \cos {}^O \gamma_S & 0 & \sin {}^O \gamma_S \\ 0 & 1 & 0 \\ -\sin {}^O \gamma_S & 0 & \cos {}^O \gamma_S \end{bmatrix} \cdot \begin{bmatrix} x_{is} \\ y_{is} \\ z_{is} \end{bmatrix} + \begin{bmatrix} {}^O x_S \\ {}^O y_S \\ {}^O z_S \end{bmatrix}$$

According to the imaging principle in the study by Trawny et al.,<sup>14</sup> the conversion relation between the coordinates  ${}^C p_{ig} = (x_{ic}, y_{ic}, z_{ic})^T$  in  $F_C$  and their image coordinates  $(u_i, v_i)^T$  can be obtained

$$\begin{bmatrix} u_i \\ v_i \end{bmatrix} = \frac{1}{z_{ic}} \begin{bmatrix} f & 0 \\ 0 & f \end{bmatrix} \begin{bmatrix} x_{ic} \\ y_{ic} \end{bmatrix} + \begin{bmatrix} c_u \\ c_v \end{bmatrix} \quad (7)$$

where  $f$  is the focal length of the camera and  $(c_u, c_v)^T$  are the principal point coordinates. These variables are obtained by camera calibration.

### Algorithm

The POSIT algorithm can estimate the object pose in a camera frame from a single image if four or more correspondences between 2-D points and 3-D points are given. The algorithm consists of two steps. First, the scaled orthographic projection is used to approximate the perspective projection and get the rotation matrix and translation vector from a set of linear equations. Second, the new scale factor is iteratively calculated for each point, and the first step is repeated using the new points instead of the original ones until the set threshold is met.<sup>15–17</sup>

Figure 4 shows the perspective projection and scaled orthogonal projection. The target frame  $F_D$  is parallel with the runway frame  $F_R$  and its origin point is the

first cooperated target  $p_{0g}$ . The points denoted by  $P_{ig}$  are the perspective projection points on the camera focal plane.  $P'_{ig}$  points are called scaled orthogonal projections.

The coordinates of the points denoted by  $p_{ig}$  in  $F_D$  and  $F_R$  have the following relation

$$\begin{bmatrix} w_i u'_i \\ w_i v'_i \\ w_i \end{bmatrix} = \begin{bmatrix} f & 0 & 0 \\ 0 & f & 0 \\ 0 & 0 & 1 \end{bmatrix} \begin{bmatrix} x_{ic} \\ y_{ic} \\ z_{ic} \end{bmatrix} = \begin{bmatrix} f & 0 & 0 \\ 0 & f & 0 \\ 0 & 0 & 1 \end{bmatrix} \begin{bmatrix} R_1 & T_x \\ R_2 & T_y \\ R_3 & T_z \\ 0 & 1 \end{bmatrix} \begin{bmatrix} x_{id} \\ y_{id} \\ z_{id} \\ 1 \end{bmatrix} = \begin{bmatrix} fR_1 & fT_x \\ fR_2 & fT_y \\ R_3 & T_z \end{bmatrix} \begin{bmatrix} {}^D p_{ig} \\ 1 \end{bmatrix} \quad (9)$$

where  ${}^C_D T = {}^C_R T + {}^C_R \cdot {}^R_D T = [T_x \ T_y \ T_z]^T$ ,  ${}^C_D R = {}^C_R \cdot {}^R_D R = {}^C_R = [R_1 \ R_2 \ R_3]$ , and  $(u'_i, v'_i)^T = (u_i, v_i)^T - (c_u, c_v)^T$ .

By introducing a range scaling factor  $s = f/T_z$ , equation (9) can be rewritten as

$$\begin{bmatrix} w_i u'_i \\ w_i v'_i \end{bmatrix} = \begin{bmatrix} sR_1 & sT_x \\ sR_2 & sT_y \end{bmatrix} \begin{bmatrix} {}^D p_{ig} \\ 1 \end{bmatrix}, \quad w_i = R_3 \cdot {}^D p_{ig} / T_z + 1, \quad (i = 1, 2, 3) \quad (10)$$

$${}^D p_{ig} = (x_{id}, y_{id}, z_{id})^T = {}^D_R R \cdot ({}^R p_{ig} + {}^R_D T) = {}^R p_{ig} + {}^R_D T \quad (8)$$

where  ${}^D_R R = I_{3 \times 3}$  and  ${}^R_D T = {}^R p_{0g}$ .

The image coordinates can be expressed as

Considering  $sT_x = fT_x/T_z = u'_0$  and  $sT_y = fT_y/T_z = v'_0$ , where  $(u'_0, v'_0)^T$  is the image coordinate of the origin of the target coordinate, equation (10) can be expressed as

$$\begin{cases} {}^D p_{ig}^T \cdot sR_1^T = w_i u'_i - u'_0 \\ {}^D p_{ig}^T \cdot sR_2^T = w_i v'_i - v'_0 \end{cases}, \quad w_i = R_3 \cdot {}^D p_{ig} / T_z + 1, \quad (i = 1, 2, 3) \quad (11)$$

The following linear equations result

$$\begin{cases} A \cdot sR_1^T = x' \\ A \cdot sR_2^T = y' \end{cases}, \quad x' = \begin{bmatrix} w_1 u'_1 - u'_0 \\ w_2 u'_2 - u'_0 \\ w_3 u'_3 - u'_0 \end{bmatrix}, \quad y' = \begin{bmatrix} w_1 v'_1 - v'_0 \\ w_2 v'_2 - v'_0 \\ w_3 v'_3 - v'_0 \end{bmatrix}, \quad A = \begin{bmatrix} x_{ir} - x_{0r} \\ y_{ir} - y_{0r} \\ z_{ir} - z_{0r} \end{bmatrix}_{3 \times 3} \quad (12)$$

Coinciding with scaled orthogonal projection, the initial values of perspective projection  $w_i (i = 1, 2, 3)$  are all equal to one. Then  $sR_1^T$  and  $sR_2^T$  can be calculated using the linear equation (12).

However, if  $z_{ir} = 0 (i = 1, 2, 3)$ , the third elements of  $sR_1^T$  and  $sR_2^T$  cannot be calculated. Let  $(I_1, I_2, I_3)^T$  and  $(J_1, J_2, J_3)^T$  represent the elements of  $sR_1^T$  and  $sR_2^T$ , respectively.  $(I_1, I_2)^T$  and  $(J_1, J_2)^T$  have been solved by

the above equation. Then, the third elements  $I_3$  and  $J_3$  satisfy the following equation

$$\begin{cases} I_3 \cdot J_3 = -I_1 J_2 + I_2 J_1 \\ I_3^2 - J_3^2 = J_1^2 + J_2^2 - I_1^2 - I_2^2 \end{cases} \quad (13)$$

Two solutions of  $I_3$  and  $J_3$  can be obtained by solving this equation. According to the characteristics of the rotation matrix

$${}^C_R R = R_y(\gamma_{r_{\mathcal{C}}}) \cdot R_x(\theta_{r_{\mathcal{C}}}) \cdot R_z(\psi_{r_{\mathcal{C}}}) = \begin{bmatrix} C_\gamma & 0 & -S_\gamma \\ 0 & 1 & 0 \\ S_\gamma & 0 & C_\gamma \end{bmatrix} \begin{bmatrix} 1 & 0 & 0 \\ 0 & C_\theta & S_\theta \\ 0 & -S_\theta & C_\theta \end{bmatrix} \begin{bmatrix} C_\psi & S_\psi & 0 \\ -S_\psi & C_\psi & 0 \\ 0 & 0 & 1 \end{bmatrix} \quad (14)$$

where  $\theta_{r_{\mathcal{C}}}$ ,  $\gamma_{r_{\mathcal{C}}}$ , and  $\psi_{r_{\mathcal{C}}}$ , respectively, represent the rotation angles from  $F_R$  to  $F_C$ ,  $C_\gamma$  is short for  $\cos(\gamma_{r_{\mathcal{C}}})$ , and  $S_\gamma$  for  $\sin(\gamma_{r_{\mathcal{C}}})$ , and so on.

In equation (14),  $J_3 = s \cdot \sin(\theta_{r_{\mathcal{C}}})$ . Note that  $s = f/T_z > 0$  and  $-p < \theta_{r_{\mathcal{C}}} < 0$  in the landing environment,

which means  $J_3 < 0$ , and the unique solution of  $I_3$  and  $J_3$  can be obtained. Now the elements of  $sR_1^T$  and  $sR_2^T$  are all worked out.

Because both  $R_1^T$  and  $R_2^T$  are unit vectors,  $s$ ,  ${}^C_R R$ , and  ${}^C_R T$  can be solved by the following equations

$$R_1^T = \frac{(sR_1^T)}{|sR_1^T|}, R_2^T = \frac{(sR_2^T)}{|sR_2^T|}, R_3^T = R_1^T \times R_2^T \quad (15)$$

$$s = \sqrt{|sR_1^T| \cdot |sR_2^T|} \quad (16)$$

$$T_x = (sT_x)/s, T_y = (sT_y)/s, T_z = f/s \quad (17)$$

As the pose estimation in the first step has been obtained, better estimations of  $w_i$  can be obtained using equation (10). Then, by substituting the new  $w_i$  estimations into the linear equation (12), we can get more accurate results. This iterative process will end when  $|w_{i(k)} - w_{i(k-1)}|$  is less than the threshold. Normalize the rotation matrix again to get the results  ${}^C_D R$  and  ${}^C_D T$ . Then,  ${}^C_R R = {}^C_D R$  and  ${}^C_R T = {}^C_D T - {}^C_R R \cdot {}^R_D T$ .

In accordance with the formulas (3) to (6), the following can be derived

$$R_z(\psi_B) \cdot {}^R_S R \cdot R_y(\gamma_S) \cdot R_x(\theta_S) = [{}^C_B R \cdot R_y(\gamma_B) \cdot R_x(\theta_B)]^{-1} \cdot {}^C_R R \cdot {}^R_S R \quad (18)$$

$${}^O_B T - {}^R_S R \cdot {}^O_S T = {}^O_S R \cdot {}^R_S T - ({}^C_B R \cdot {}^B_O R)^{-1} \cdot {}^C_R T - {}^R_S R \cdot {}^S_R T + {}^O_P R \cdot {}^B_C T \quad (19)$$

The right-hand side of equation (18) is formed by known values, so  $\psi_B$ ,  $\gamma_S$ ,  $\theta_S$ , and the entire rotation matrix can be calculated. Assume that  ${}^O_{x_S} = {}^O_{y_S} = 0$ , then through equation (19),  $[{}^O_{x_B} \quad {}^O_{y_B} \quad {}^O_{z_B} - {}^O_{z_S}]^T$  can be obtained. The entire process of applying the algorithm is shown in Figure 5.  $\theta_{B\_INS}$  and  $\gamma_{B\_INS}$  represent the pitch and roll angle from the airborne INS, respectively.  $z_{B\_Ra}$  represents the height of the aircraft from the radio altimeter.

### Control law

The optimal linear quadratic regulator (LQR) is employed in this study. LQR is a common method to analyze multiple-input multiple-output FCS in modern control theory.<sup>18</sup>

The reference trajectory can be calculated according to the aircraft carrier motion ( $\gamma_S$ ,  $\theta_S$ , and  $z_S$ ). Then, the off-glide-path lateral distance  $d_x$ , vertical distance  $d_z$  (both refer to modified reference trajectory), and velocity  $V$  are obtained as inputs to the control law. The control objective is to regulate these variables to a value of zero for keeping the aircraft on the glide path. Therefore, the vertical state vector  $x_v$  and the lateral state vector  $x_l$  can be expressed as follows

$$\begin{aligned} x_v &= [V; \alpha; \theta; q; d_z; ] \\ x_l &= [\beta; \phi; p; r; d_x; ] \end{aligned} \quad (20)$$

where  $\alpha$ ,  $\beta$ ,  $\theta$ ,  $\phi$ ,  $q$ ,  $p$ , and  $r$  are the attack angle, sideslip angle, pitch angle, bank angle, pitch rate, roll rate, and yaw

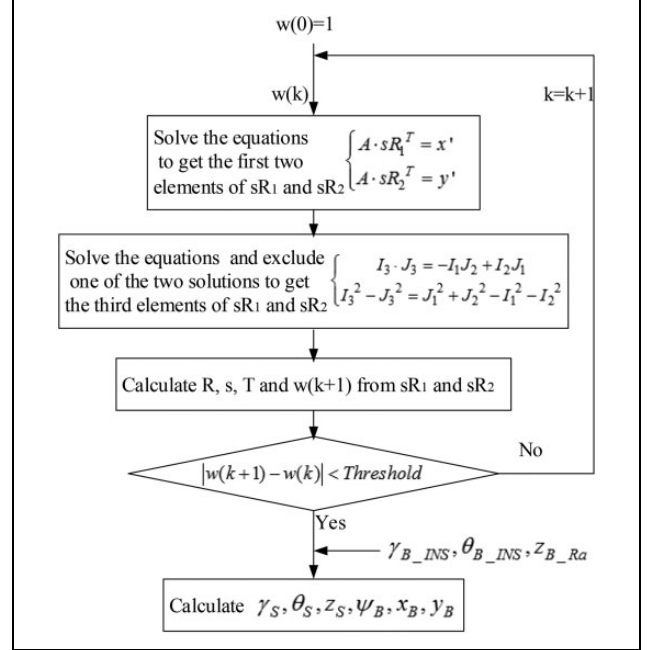


Figure 5. The schematic of the algorithm application.

rate, respectively. States of the aircraft are observable by using aircraft sensors.

The control vector is defined as

$$u = [u_v; u_l] = [\delta_t; \delta_e; \delta_r; \delta_a;] \quad (21)$$

where  $\delta_t$ ,  $\delta_e$ ,  $\delta_a$ , and  $\delta_r$  are throttle, elevator, aileron, and rudder deflections, respectively. In the control vector, the throttle and elevator deflections are used for aircraft vertical control, and rudder and aileron deflections are used for aircraft longitudinal control. State feedback is utilized and the control inputs are computed as follows

$$\begin{bmatrix} u_v \\ u_l \end{bmatrix} = - \begin{bmatrix} K_v & 0_{2 \times 7} \\ 0_{2 \times 7} & K_l \end{bmatrix} \begin{bmatrix} \tilde{x}_v \\ \tilde{x}_l \end{bmatrix} \quad (22)$$

where  $K_v$  and  $K_l$  are state feedback gains. The optimal LQR method is used to compute the state feedback gains with the weighting matrix defined by Brian and Frank<sup>18</sup>

$$\begin{aligned} Q &= \text{diag}(1/\tilde{x}_{i\_max}^2) \\ R &= \text{diag}(1/\tilde{u}_{i\_max}^2) \end{aligned} \quad (23)$$

### Simulation

A simulation is discussed for validating the performance of the visual/inertial integrated landing guidance algorithm. In this experiment, the aircraft carrier is assumed to move at a speed of 20 knots (about 10.3 m s<sup>-1</sup>), with governed by classic carrier dynamics.<sup>19–22</sup> The simulation starts when the aircraft is 1500 m away from the aircraft carrier. The aircraft model in this control law simulation is assumed to be F-14. The carrier model is assumed to be the American Nimitz-class aircraft carrier, and the coordinates of the

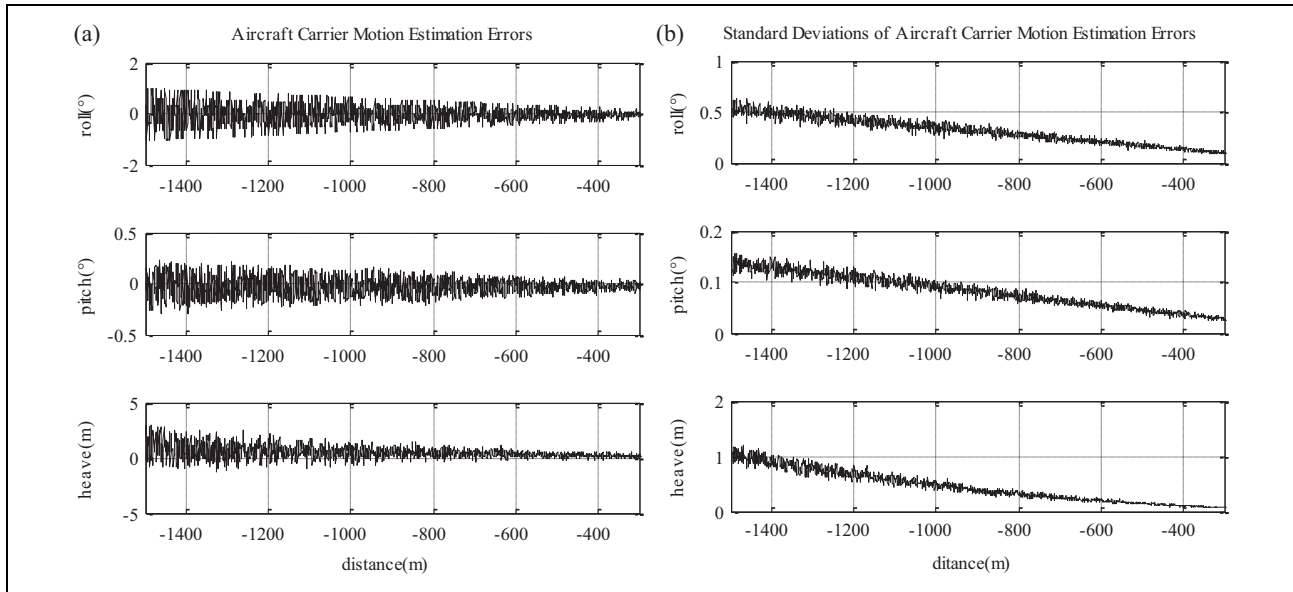


**Figure 6.** (a) The aircraft carrier motion estimation errors in one landing phase, including the roll, pitch, and heave and (b) the standard deviations of the aircraft carrier motion estimation errors calculated from 20-time carrier landing.

cooperated targets in the carrier runway frame are (15, -65, 0), (-15, -65, 0), (15, 175, 0), and (-15, 175, 0), respectively. Sea-state level 3 in the study by Sweger<sup>19</sup> is chosen as the experimental condition. The root mean square (RMS) amplitudes of the heave, roll, and pitch are 0.91 m, 0.32°, and 1.08°, respectively. The air wake is considered using the model in the American Air Force manned aircraft flight quality specifications MIL-F-8785C.

The resolution and field of view of the vision system are  $768 \times 576$  and  $8^\circ \times 6^\circ$ , respectively, whereas the output frequency is 25 Hz. The focal length calibration errors of the vision system are less than 0.2%. The target coordinate extracting errors are less than two pixels, and they decrease as the distance between the aircraft and the carrier decreases. The INS is assumed to have initial errors in attitude, velocity, and position measurements, and the drift error of the gyroscopes is  $0.01^\circ \text{ h}^{-1}$ , whereas the accuracy of the accelerometers is 50  $\mu\text{g}$ .

### Guidance performance

The guidance simulation involves estimating the carrier motion as well as the relative position between the aircraft and the carrier. Figure 6(a) and (b) shows the aircraft carrier motion estimation errors and standard deviations. Figure 7(a) and (b) shows the aircraft motion estimation errors and standard deviations. The horizontal axes in these figures are the real longitudinal distances between the aircraft and the carrier.

As shown in Figures 6 and 7, the initial estimation errors exist because of the initial attitude error from the INS, the focal length error, and so on. As the aircraft approaches the carrier, the estimation errors reduce in value. When the distance between the aircraft and the carrier is less than

400 m, the aircraft position estimation errors converge to 0.5 m in lateral distance, 0.8 m in vertical distance, 2.5 m in longitudinal distance, and  $0.1^\circ$  in the heading angle estimation. The carrier motion angle estimation error is less than  $0.2^\circ$ , whereas the heave estimation error is less than 0.8 m.

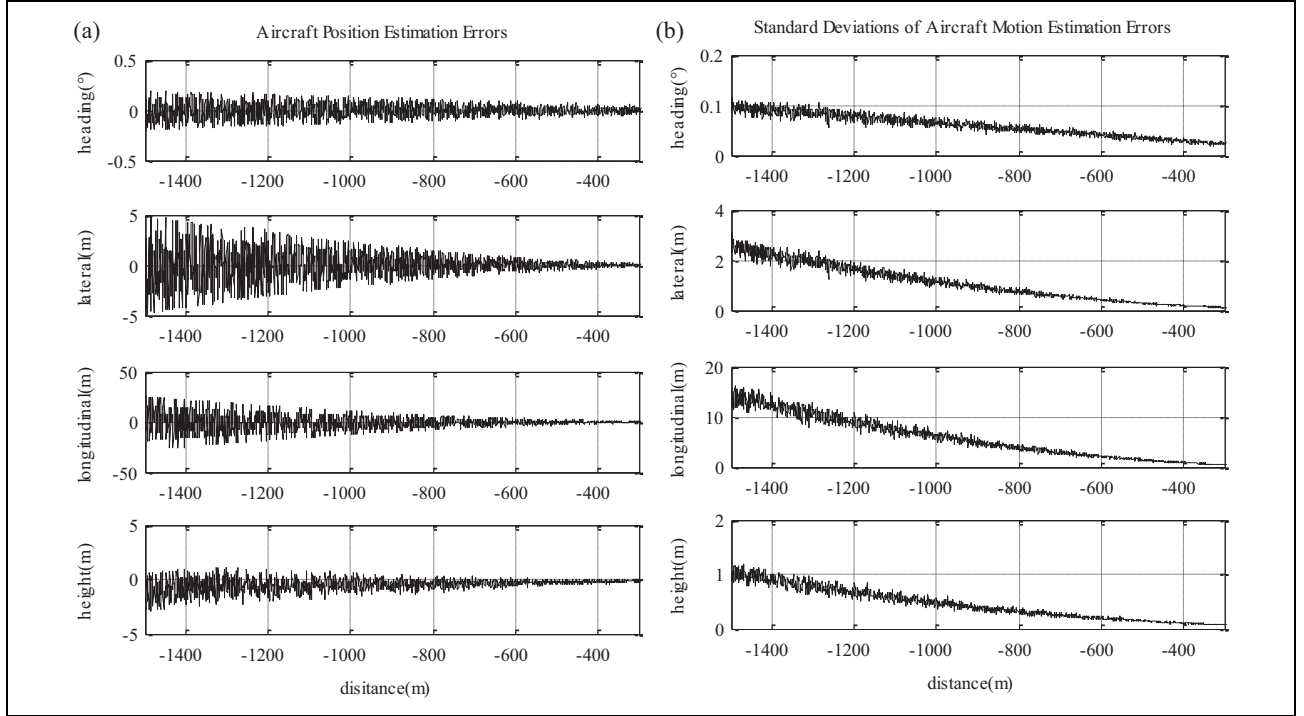
Several algorithms that can be utilized in vision-based carrier landing guidance system have been researched. For comparison, Newton's iterative algorithm, an algorithm from École Polytechnique Fédérale de Lausanne (EPFL algorithm), and the planar homography algorithm have also been studied. The details of the other three algorithms can be found in the works of Ding et al.,<sup>13</sup> Hajri,<sup>17</sup> and Moreno-Noguer et al.<sup>22</sup> and Yang et al.,<sup>23</sup> respectively.

Table 1 lists the data obtained by simulating the carrier landing 20 times and presents the max and standard deviation of estimation errors, and the max and average values of execution time when the longitudinal distance between the aircraft and the carrier is 400 m. As presented in Table 1, the estimation error of the algorithms based on EPFL and planar homography is too large to meet the landing requirements, so the standard deviations of the estimation errors of those two algorithms are not given.

The algorithm proposed in this article has advantages in terms of the execution time and comparative accuracy when compared with Newton's iterative algorithm. Considering the difficulty of the engineering application, execution time, and estimation accuracy, the algorithm in this article is slightly better than Newton's iterative algorithm.

### Control law

The simulation for the control law validation is discussed subsequently. Figure 8(a) shows the aircraft lateral



**Figure 7.** (a) The aircraft motion estimation error, including the relative heading angle, the relative lateral position, longitudinal position, and height and (b) the standard deviations of the aircraft motion estimation errors calculated from 20-time carrier landing.

**Table 1.** Comparison of the estimation results using the four algorithms.

		Algorithm based on POSIT	Newton's iterative algorithm	Algorithm based on EPFL	Algorithm based on planar homography
Execution time (ms)	Max	0.28	0.45	1.57	1.60
	Avr	0.24	0.29	1.11	1.13
Carrier roll (°)	Max	0.312	0.332	1.050	1.050
	Std	0.119	0.141	—	—
Carrier pitch (°)	Max	0.068	0.090	0.335	0.335
	Std	0.031	0.034	—	—
Lateral distance (m)	Max	0.25	0.22	208.05	102.66
	Std	0.15	0.13	—	—
Longitudinal distance (m)	Max	1.30	1.23	28.92	30.37
	Std	0.62	0.65	—	—
Relative height (m)	Max	0.35	0.35	1.71	1.39
	Std	0.09	0.09	—	—
Relative heading (°)	Max	0.050	0.043	15.477	15.477
	Std	0.025	0.021	—	—

POSIT: Pose from Orthographic Projection and Scaling with Iterations; EPFL: École Polytechnique Fédérale de Lausanne; Max: maximum; Avr: average; Std: standard deviation.

position  $s_{x_B}$  in the carrier body frame  $F_S$  and the off-glide-path lateral distance  $d_x$ , respectively, when the aircraft is landing on the aircraft carrier using the control law. Figure 8(b) shows the aircraft height  $s_{z_B}$  and the off-glide-path vertical distance  $d_z$ . The results of the aircraft lateral and vertical control response can converge to 0.5 m in terms of position errors.

## Conclusion

In this article, a new visual/inertial integrated carrier landing guidance algorithm based on POSIT was designed to calculate the aircraft pose and carrier motion in the carrier landing operation. The simulation performed using this algorithm was discussed for validation, and the results show that this algorithm performs precisely with respect



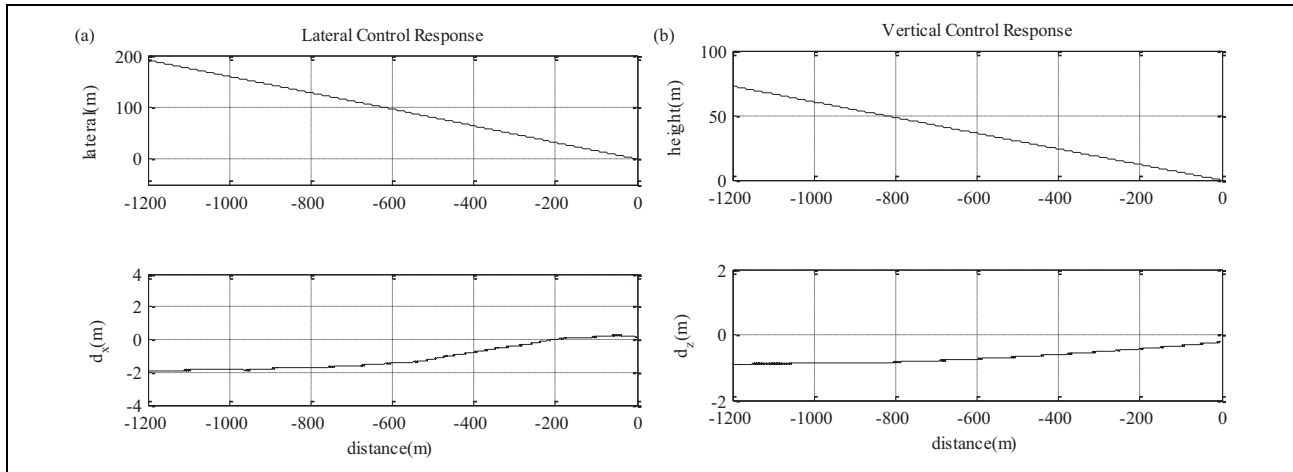


**Figure 8.** (a) The aircraft lateral position in the carrier body frame and the off-glide-path lateral distance and (b) the aircraft height in the carrier body frame and the off-glide-path vertical distance.

to calculating landing estimates and satisfactory control response. On comparing simulation results across algorithms, it is obvious that this algorithm has unique advantages in terms of the execution time, comparative accuracy compared with Newton's iterative algorithm, and much better performance than that of the algorithms based on EPFL and planar homography. These results can be applied in carrier landing operations.

### Declaration of conflicting interests

The author(s) declared no potential conflicts of interest with respect to the research, authorship, and/or publication of this article.

### Funding

The author(s) received no financial support for the research, authorship, and/or publication of this article.

### ORCID iD

Yue Meng  <http://orcid.org/0000-0002-3052-3094>

### References

- Crassidis JL, Mook DJ, and Mcgrath JM. Automatic carrier landing system utilizing aircraft sensors. *J Guid Control Dyn* 1993; 16(5): 914–921.
- Zhimin H and Guanxin H. Modeling and simulation on error sources of the designating system for fully automatic carrier landing. *Res J Appl Sci Eng Technol* 2013; 5(11): 3117–3123.
- Wenling Z, Wenhai W, and Gaofeng A. Dissimilar redundancy structure design for carrier landing guidance computer and reliability analysis. *Lecture Notes Electr Eng* 2014; 297(2): 379–385.
- Sousa P, Wellons L, Colby G, et al. *Test results of an F/A-18 automatic carrier landing using shipboard relative global positioning system*. Patuxent River, Maryland: Naval Air Warfare Center Aircraft Division. Rep. NAWCADPAX/RTR-2003/122, 2003.
- Schug EC, Aksteter JW, Huff RW, et al. Guidance and control for shipboard automatic landing using GPS. In: *Proceedings of ION 57th annual meeting/CIGTF 20th biennial guidance, test symposium*, Albuquerque, NM, 11–13 June 2001, pp. 852–862.
- Sharp CS, Shakernia O, and Sastry SS. A vision system for landing an unmanned aerial vehicle. In: *Proceedings of international conference on robotics and automation*, Seoul, Korea, 21–26 May 2001, Vol. 2, pp. 1720–1727. IEEE.
- Saripalli S, Montgomery JF, and Sukhatme GS. Visually guided landing of an unmanned aerial vehicle. *IEEE Trans Robot Autom* 2003; 19(3): 371–381.
- Gui Y, Guo P, Zhang H, et al. Airborne vision-based navigation method for UAV accuracy landing using infrared lamps. *J Intell Robot Syst* 2013; 72(2): 197–218.
- Anitha G and Kumar RG. Vision based autonomous landing of an unmanned aerial vehicle. *Procedia Eng* 2012; 38: 2250–2256.
- Yakimenko OA, Kaminer II, Lentz WJ, et al. Unmanned aircraft navigation for shipboard landing using infrared vision. *IEEE Trans Aerosp Electron Syst* 2002; 38(4): 1181–1200.
- Coutard L and Chaumette F. Visual detection and 3D model-based tracking for landing on an aircraft carrier. In: *Proceedings of international conference on robotics and automation, ICRA*, Shanghai, China, 9–13 May 2011, pp. 1746–1751. IEEE.
- Coutard L, Chaumette F, and Pflimlin JM. Automatic landing on aircraft carrier by visual servoing. In: *Proceedings of international conference on intelligent robots and systems, IROS*, San Francisco, CA, USA, 25–30 September 2011, pp. 2843–2848. IEEE.
- Ding Z, Li K, Meng Y, et al. FLIR/INS/RA integrated landing guidance for landing on aircraft carrier. *Int J Adv Robot Syst* 2015; 12(5): 1–9.
- Trawny N, Mourikis AI, Roumeliotis SI, et al. Vision-aided inertial navigation for pin-point landing using observations of mapped landmarks. *J Field Robot* 2007; 24(5): 357–378.



15. Dementhon DF and Davis LS. Model-based object pose in 25 lines of code. *Int J Comput Vis* 1995; 1 5(1–2): 123–141.
16. Oberkamp D, DeMenthon DF, and Davis LS. Iterative pose estimation using coplanar feature points. *Computer Vision and Image Understanding* 1996; 63(3): 495–511.
17. Hajri R. *UAV to UAV target detection and pose estimation*. Doctoral dissertation, Naval Postgraduate School, Monterey, California, 2012.
18. Brian LS and Frank LL. *Aircraft control and simulation*. Hoboken, New Jersey, USA: John Wiley & Sons Inc, 1992.
19. Sweger JF. *Design Specifications development for unmanned aircraft carrier landings: A simulation approach*. U.S.N.A., Trident Scholar project report. Report no. 316, 1–71, 2003. The Rubicon Research Repository.
20. Haitao Y, Xinmin W, and Wenchao L. Study of disturbances model on carrier-based aircraft landing process. *Appl Mech Mater* 2013; 321: 824–828.
21. Deyi S, Jianjun Z, and Yi W. Carrier rocking motion model based on stress analysis. *Appl Mech Mater* 2014; 667: 430–436.
22. Moreno-Noguer F, Lepetit V, and Fua P. Accurate non-iterative  $O(n)$  solution to the PnP problem. In: *Proceedings of 11th international conference on computer vision*, Rio de Janeiro, Brazil, 14–21 October 2007. ICCV, pp. 1–8. IEEE.
23. Yang Y, Qixin C, Charles L, et al. Pose estimation based on four coplanar point correspondences. In: *Proceedings of the FSKD 2009 sixth international conference on fuzzy systems and knowledge discovery*, Tianjin, China, 14–16 August 2009, Vol. 5, pp. 410–414. IEEE.